COMMUNICATIONS IN SCIENCE AND TECHNOLOGY
Homepage: cst.kipmi.or.id

Formation and stability investigation of *meso*-hydroxy diacyl-dipyrromethane

Mohammad Akbar Ferryansyah[a], Anas Santria[b,c], Naoto Ishikawa[b], Dikhi Firmansyah[a,*]

[a]*Organic Chemistry Division, Department of Chemistry, Faculty of Mathematics and Natural Sciences, Institut Teknologi Bandung, Bandung 40132, Indonesia*
[b]*Department of Chemistry, Graduate School of Science, The University of Osaka, Osaka 560-0043, Japan*
[c]*Research Center for Chemistry, National Research and Innovation Agency, Tangerang Selatan 15314, Indonesia*

Article history:
Received: 1 December 2024 / Received in revised form: 5 March 2025 / Accepted: 8 March 2025

Abstract

The oxidation of dipyrromethane by 2,3-dichloro-5,6-dicyano-1,4-benzoquinone (DDQ) generally produces dipyrrin, but in the presence of trace water, a *meso*-hydroxy dipyrromethane can be formed. To investigate this unusual product, we then studied *meso*-hydroxy bis(*p*-anisoyl)-*p*-fluorophenyl dipyrromethane (**3**) obtained from the oxidation of bis(*p*-anisoyl)-*p*-fluorophenyl dipyrromethane (**2**). Spectroscopic studies (^{1}H-NMR, UV-Vis, and fluorescence), mass spectrometry, and computational analyses were performed to investigate this mechanism. Zinc complexation of compound **3** altered the 1H-NMR spectrum and shifted the absorption peak from 325 nm to 567 nm with "turn-on" fluorescence. Thermochemical studies have indicated that the formation of *meso*-hydroxy requires energy higher than dipyrrin. This study suggests that the electronic properties of meso-aryl and acyl groups are the key factors for the nucleophilic attack of water on cationic dipyrromethane intermediate. These results further improve the understanding of dipyrromethane oxidation pathways, which is crucial for the design and synthesis of dipyrrin-chemosensors.

Keywords: Acyl dipyrromethene; DDQ oxidation; zinc dipyrrin complex; computational study

1. Introduction

Dipyrromethane (DPM) is widely used as a precursor for functional oligopyrrole, including porphyrins and calixpyrroles, as well as dipyrrin and its metal-dipyrrin complexes. Dipyrrins can be obtained through the dipyrromethane oxidation using an oxidant such as 2,3-dichloro-5,6-dicyano-1,4-benzoquinone (DDQ) or 2,3,5,6-tetrachloro-1,4-benzoquinone (*p*-chloranil) [1-4]. These compounds and their derivatives have potential applications in bioimaging, and photodynamic therapy, and act as pigments in dye-sensitized solar cells [5-9]. Dipyrromethane has also been used as a catalyst in olefin hydroamination and hydrogen transfer reactions [10-11].

Among these, acyl dipyrrin has been reported as a potential chemosensor for zinc (II) ions with chelation-enhanced fluorescence (CHEF) "turn-on" process [12-13]. Inadvertently, some diacyl dipyrromethanes produced meso-hydroxy DPM through the oxidation of dipyrromethanes using DDQ [14-16]. These compounds were proposed to be obtained *via* the formation of a carbocation intermediate reacting with trace water. Upon closer inspection, *meso*-hydroxy diacyl dipyrromethane exhibited slower complexation, then rising a question regarding the stability of this DPM compared to the dipyrrin species.

In this study, we report the formation of a *meso*-hydroxy acyl dipyrromethane derivative using NMR and MS with a focus on the effects of the *meso*- and diacyl substituents. The fluorine and anisoyl groups offer the unique duality of inductive electron-withdrawing and mesomeric electron-donating effects. UV-vis and fluorescence measurements were performed to observe the optical properties of the zinc(II) complex. We also employed computational methods using density functional theory (DFT) to examine the thermochemical and electronic parameters of all intermediates and products involved in the formation of *meso*-hydroxy acyl dipyrromethane and compared these results with those of known DPM derivatives. These findings contribute to a deeper understanding of the formation, stability, and complexation of *meso*-hydroxy acyl dipyrromethanes and their potential applications.

2. Materials and Methods

2.1. Chemicals and reagents

Commercially available solvents and reagents from Aldrich

* Corresponding author.
email: dikhfi@itb.ac.id
https://doi.org/10.21924/cst.10.1.2025.1593

were used as received. The crude product was purified by column chromatography on silica gel 60G (70–230 mesh ASTM; Merck) and monitored by thin-layer chromatography (TLC) using silica gel 60 F_{254} (Merck).

2.2. Synthesis

Fig. 1 depicts the synthetic route to *meso*-hydroxy *bis*(*p*-anisoyl)-*p*-fluorophenyl dipyrromethane (**3**). The structures of *p*-fluorophenyl dipyrromethane (**1**) and b*is*(*p*-anisoyl)-*p*-fluorophenyl dipyrromethane (**2**) were identified by ^{1}H NMR and ^{13}C spectroscopy by means of an Agilent DD2 instrument. ^{1}H-NMR spectra recorded with a JEOL ECZS confirmed the structure of compound **3** and the identification of its zinc complex, Zn-**3**. Compound **3** was characterized using MALDI-MS in the positive linear mode on a Shimadzu AXIMA Performance instrument with dithranol as the matrix. Furthermore, HRMS measurements in positive mode by means of ESI-TOF Waters LCT Premier XE were carried out to verify the presence of compound **3**. Compound **1** was synthesized following a previously reported procedure, and its spectroscopic data were consistent with those reported previously [17].

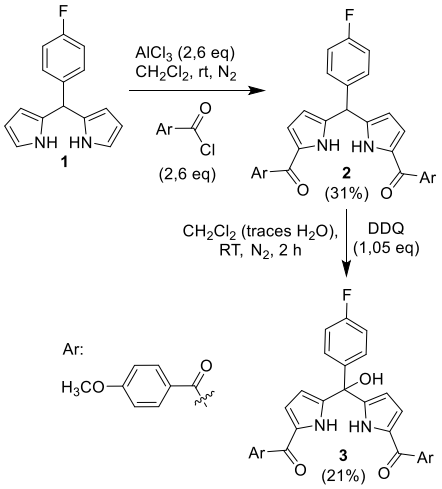

Fig. 1. Synthesis of *meso*-hydroxy bis(*p*-anisoyl)-*p*-fluorophenyl dipyrromethane

2.2.1. Synthesis of bis(p-anisoyl)-p-fluorophenyl dipyrromethane (2)

Compound **2** was prepared in accordance to a modified literature procedure [13]. It began by adding 72 mg (0.54 mmol, 2.57 eq) of $AlCl_3$ to a solution of *p*-anisoyl chloride (96 mg, 0.56 mmol, 2.67 eq) in 5.2 mL dichloromethane. The mixture was then stirred for 30 min under an inert nitrogen atmosphere at room temperature. Subsequently, a solution of compound **1** (51 mg, 0.21 mmol, 1 eq) in 1.3 mL dichloromethane was added slowly, and the reaction continued for 2 h. Upon completion, 8 mL of distilled water was added, the mixture was extracted, the organic layer was collected, and the solvent was removed under reduced pressure. The resulted brown solid was purified on silica gel using a dichloromethane: ethyl acetate (19:1) eluent to afford a brown solid product (32.9 mg, 30.8%). ^{1}H NMR (500 MHz, $CDCl_3$) δ (ppm) 3.85 (6H, *s*, H-methoxy), 5.67 (1H, *s*, H-*meso*), 5.89 (2H, *s*, H-pyrrole), 6.47-6.49 (2H, *m*, H-pyrrole), 6.90 (4H, d, ^3J = 8.8 Hz, H-benzoyl), 7.09 (2H, *t*, ^3J = 8.6 Hz, H-phenyl), 7.54-7.58 (2H, *dd*, ^3J = 8.4 Hz and ^4J 5.4 Hz, H-phenyl), 7.77 (4H, *d*, ^3J = 8.8 Hz, H-benzoyl), and 11.94 (2H, broad *s*, NH). ^{13}CNMR (125 MHz, $CDCl_3$) δ (ppm) 44.3 (CH-*meso*), 55.4 (OCH_3), 111.0 (CH-pyrrole), 113.3 (CH-benzoyl), 115.5 and 115.7 (*d*, ^2J = 21.3 Hz, CH-phenyl), 120.1 (CH-pyrrole), 130.5 (*d*, ^2J = 8.8 Hz, CH-phenyl), 130.9 (C_q-pyrrole), 131.1 (C_q-benzoyl), 131.8 (CH-benzoyl), 136.5 (*d*, ^4J = 3.8 Hz, C_q-phenyl), 140.5 (C_q-pyrrole), 161.1 and 163.1 (*d*, ^4J = 245.0 Hz, C_q-F-phenyl), 162.5 (C_q-O-benzoyl), and 183.4 (C=O).

2.2.2. Synthesis of meso-hydroxy bis(p-anisoyl)-p-fluorophenyl dipyrromethane (3)

The oxidation of acyl dipyrromethane was conducted following a previously reported procedure [18]. A solution of compound **2** (30 mg, 0.059 mmol, 1 eq) in 6 mL CH_2Cl_2 was added to a flask containing DDQ (14 mg, 0.062 mmol, 1.05 eq) and stirred for 2h. Once it was complete, the solvent was removed *in vacuo*. The residue was purified by column chromatography on silica gel using a dichloromethane:ethyl acetate (49:1) eluent and recrystallized from methanol to yield 6.5 mg (21%) of a reddish-white solid. The ^{1}H NMR (400 MHz, $CDCl_3$) revealed signals at δ (ppm) 3.87 (6H, *s*, H-methoxy), 5.89-5.91 (2H, *dd*, ^3J = 3.8 Hz and ^4J = 2.6 Hz, H-pyrrole), 6.07 (1H, broad *s*, OH-*meso*), 6.66-6.69 (2H, *dd*, ^3J = 3.8 Hz and ^4J = 2.5 Hz, H-pyrrole), 6.92-6.95 (4H, *d*, ^3J = 8.9 Hz, H-benzoyl), 6.97-7.02 (2H, *t*, ^3J = 8.8 Hz, H-phenyl), 7.39-7.44 (2H, *dd*, ^3J = 8.9 Hz and ^4J = 5.3 Hz, H-phenyl), 7.74-7.79 (4H, *d*, ^3J = 8.9 Hz, H-benzoyl), and 11.08 (2H, broad *s*, NH). HRMS-ESI found 547.1646, calculated 547.1645 for $[M + Na]^+$ ($C_{31}H_{25}FN_2NaO_5^+$).

2.3. Zinc complexation

For the UV–Vis studies, a 10 µM solution of compound **3** was prepared in methanol (Merck, analytical grade). Aliquots of 200 µM acetate standard solutions of Zn^{2+} were added to methanol. UV–vis titrations were performed using an Evolution™ 220 UV-Visible Spectrophotometer (Thermo Scientific) with a 1 cm quartz cuvette at 20°C, while separate complex formation after 24 h was performed with the help of a UV-vis Perkin Elmer Lambda 25 UV-Vis Spectrophotometer. The zinc complex (see Fig. 2) was prepared by adding excess $Zn(OAc)_2{\cdot}2H_2O$ (4.5 mg, 10 eq) to a vial containing 1 mg of compound **3** dissolved in 254.5 µL of methanol to ensure the completion of the complexation. The mixture was sonicated for 5 min until reaching full dissolution and it was then left at room temperature for 24 h. After the solvent was removed under reduced pressure, a magenta solid (5.5 mg) was obtained. The dried sample was re-dissolved to a concentration of 10 µM in methanol, and the UV-vis spectra were measured. The structure of **Zn-3** (zinc complex) was identified by ^{1}H-NMR spectroscopy (Jeol). MS was carried out in the linear positive mode using MALDI-TOF (Shimadzu) with dithranol as the matrix. Furthermore, the emission spectra of the zinc complexes were measured using a Duetta™ fluorescence and absorbance spectrometer (Horiba).

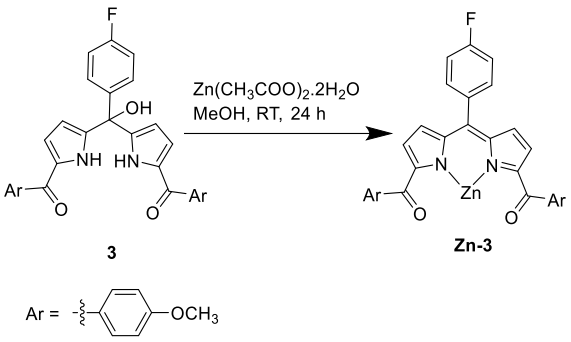

Fig. 2. Complexation of **3** with zinc acetate (10 eq) for 24 h

2.4. Computational method

Molecular structures were modelled using BIOVIA TmoleX 2023 (version 23.1.0) [19] and Turbomole version 7.7.1. [20]. Pre-optimization was first achieved using the GFN2-xTB method [21], followed by complete geometry optimization using DFT with the B3-LYP functional [22-23], def2-TZVP basis set [24], and DFT-D4 dispersion correction. TD-DFT calculations in Turbomole were used for electronic and excited state analyses, employing the similar functional, basis set, and dispersion correction as in the geometry optimization. BIOVIA TmoleX provided the visualization of the molecular orbitals and energy levels. Thermochemical parameters were further calculated from frequency calculations using Turbomole with parameters analyzed using a BIOVIA TmoleX 2023.

3. Results and Discussion

3.1. Synthesis and characterization

The *para*-fluorophenyl substituent at the *meso* position, along with the anisoyl group, was selected with a consideration to its mesomeric electron donor nature, helping in stabilizing the carbocation intermediate. Additionally, fluorine's high electronegativity and small atomic radius allowed it to mimic the behavior of hydrogen and hydroxy group.[25] Compound **1** was successfully synthesized as a precursor of compound **2** with the yield of 66.5%. Dipyrromethane **1** was characterized by ^{1}H NMR and identified by *meso*-proton signal at 5.48 ppm, pyrrole signal in the range of 5.90 to 6.74 ppm, and NH signal at 7.94 ppm. The disubstituted aromatic pattern exhibited ortho-coupling (~8 Hz), confirming the expected substitution pattern. The Friedel-Craft acylation of **1** using anisoyl chloride yielded acyl dipyrromethane **2** by 30.8%. The proton NMR spectrum of compound **2** displayed additional signals corresponding to the anisoyl substituent with benzoyl protons appearing at 7.77 ppm and 6.90 ppm, and a methoxy signal at 3.85 ppm. The N-H pyrrole proton was deshielded after acylation (from 7.94 ppm to 11.91 ppm). This might be due to the hydrogen bonding between the N-H and oxygen from benzoyl C=O. Furthermore, the loss of one signal of H-pyrrole in the α-position confirmed successful acylation.

Compound **3** was synthesized by the oxidation of **2** using DDQ, followed by purification via silica gel chromatography and recrystallization from methanol, resulting in the yield of 21%. The proton NMR characterization revealed minimal shifts in the pyrrole proton signals, while the NH proton exhibited shielding, shifting from 11.94 ppm to 11.08 ppm. In addition, the *meso*-proton signal, initially observed as a sharp singlet at 5.67 ppm, shifted to a broad singlet at 6.07 ppm, indicating the formation of *meso*-OH (Fig. 3).

HRMS-ESI data further confirmed the formation of **3** $[M+Na]^+$ at m/z 547.1645. However, the MALDI-TOF MS data revealed high-intensity peaks tentatively identified as DPM (**2**) at m/z 509.0765 (calculated 509.1871, $[M+H]^+$) and dipyrrin (**3'**) at m/z 506.9570 (calculated 507.1715, $[M+H]^+$), along with a lower intensity peak for compound **3** at m/z 525.0284 (calculated 525.1820, $[M+H]^+$). These results indicate that in ionic forms the DPM and dipyrrin are more stable than the *meso*-hydroxy species.

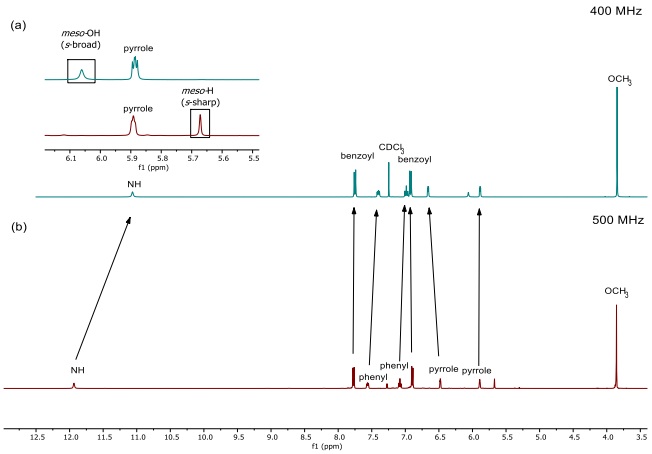

Fig. 3. Comparison of ^{1}H NMR spectra of (a) **3** and (b) **2**

3.2. Spectroscopic studies of Zinc complexation

The non-conjugated system of compound **3** resulted in a maximum absorption wavelength λ_{max} at 325 nm (Fig. 4), shorter than that of dipyrrins (400-500 nm) such as allyl-vanillin dipyrrin (476 nm) [26]. Upon complexation with zinc(II), a new absorption peak was observed at 567 nm, expected for the complex with dipyrrin ligand. The isosbestic point was monitored at 357 nm, indicating complexation with zinc(II) ions. However, even after the addition of 20 eq. molar of zinc(II) ions, the intensity of complex remained lower than that of the ligand.

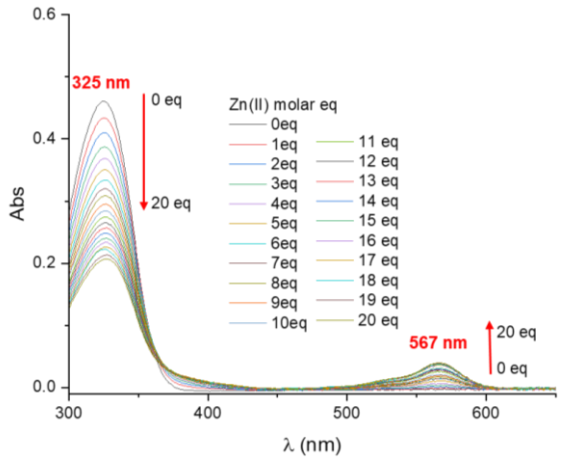

Fig. 4. Complexation of 10 μM **3** with 200 μM $Zn(CH_3COO)_2$ 0-20 eq molar in methanol and temperature of 20°C

After allowing the mixture to stand for 24 h, the absorption intensity of the zinc(II) complex at 567 nm significantly increased (Fig. 5). This suggested a slow complexation process between ligand **3** and zinc(II) due to the formation of dipyrrin as the true ligand. The emission of the zinc complex was also measured and an emission peak was detected at 606 nm (Fig. 6). Further confirmation of complex formation was provided by MALDI-TOF MS where the peaks at 570.0067 and 507.0915 were observed, which closely agreed with $[(\mathbf{Zn\text{-}3})+H]^+$ (calculated 570.0933) and dipyrrin $[\mathbf{3}+H]^+$ (calculated 507.1715).

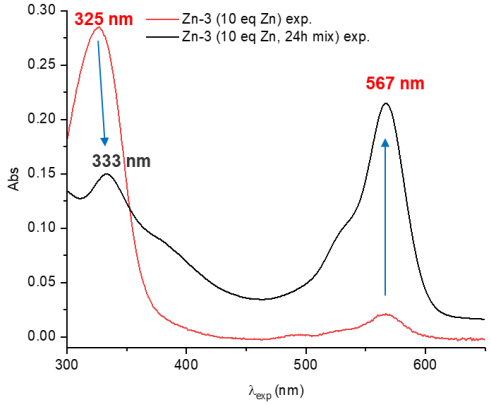

Fig. 5. UV-vis spectra of **3** with 20 eq Zn(II) measured spontaneously and **3** with 10 eq Zn(II) measured after 24 h

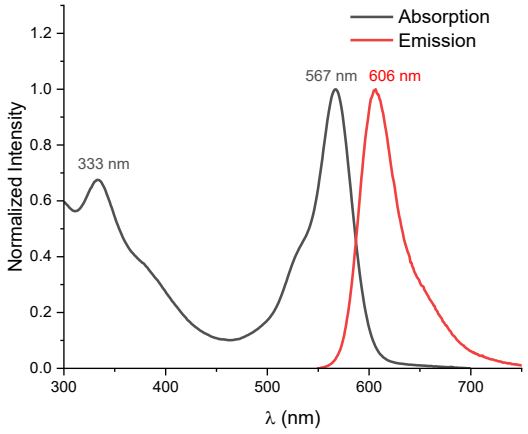

Fig. 6. Normalized absorption and emission spectra of **Zn-3**

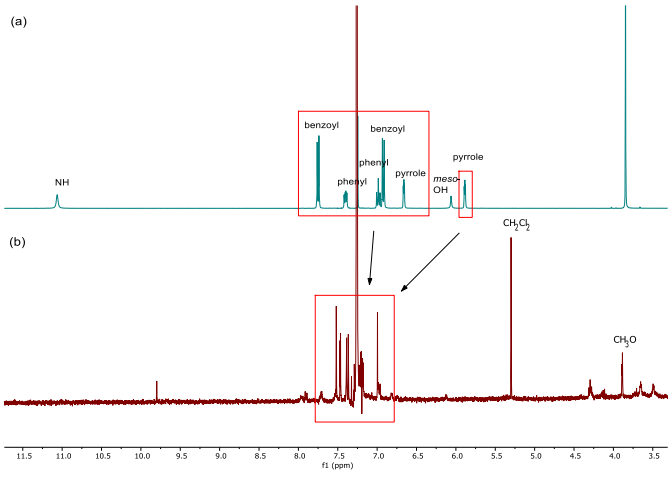

Fig. 7. Comparison of ^{1}H NMR spectra of (a) **3** and (b) **Zn-3** in $CDCl_3$

The ^{1}H NMR spectrum of the **Zn-3** complex showed indistinct multiplicity and integration patterns; however, the notable chemical shifts provided valuable insights. When comparing the spectra of **3** to **Zn-3** (Fig. 7), the pyrrole protons exhibited a downfield shift, similar to the behavior as observed during the oxidation of dipyrromethanes to dipyrrins. This shift indicated that a dipyrrin-zinc(II) complex was successfully formed. These NMR results corroborated the UV-vis data, showing the development of a dipyrrin ligand after the complexation of *meso*-hydroxy dipyrromethane **3** with zinc(II).

Moreover, the disappearance of the *meso*-OH signal post-complexation indicated the absence of OH at the *meso*-C position and the formation of a conjugated structure at this site. While other signals were not individually identifiable, notable changes in the chemical shift ranges of benzoyl and phenyl were observed. Specifically, the signal range shifted slightly from 6.9-7.9 ppm to 6.9-7.6 ppm in **Zn-3**, indicating subtle structural modifications upon complexation.

3.3. Computational study

The TD-DFT electronic transition calculations were compared with the experimental UV-vis spectra (Fig. 8). Before complexation, the absorbance profile of the ligand closely aligned with the calculated profile of structure **3**, rather than that of structure **3'**. The primary absorbance peak corresponded to the fourth electronic transition, involving a transition from the π system of pyrrole-phenyl-benzoyl (HOMO) to the π* orbital of pyrrole-benzoyl (LUMO+1).

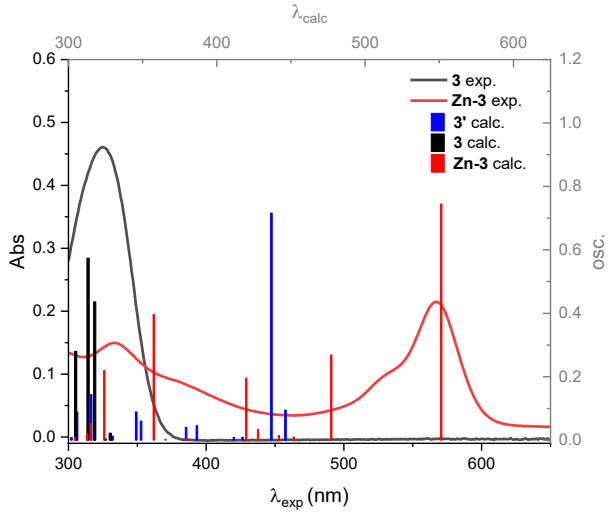

Fig. 8. Comparison of calculated oscillator strength data and experimental absorbance data of **3**, **3'**, and **Zn-3**

After complexation with zinc(II), the absorbance profile of the complex matched the calculated profile of **Zn-3**. The dominant peak arose from the first electronic transition, which corresponded to the π system of the pyrrole-benzoyl (HOMO) transitioning to the π* orbital of the pyrrole (LUMO). This shift in the absorption pattern suggests that complexation induces a structural conversion of the ligand from structure **3** to structure **3'**, aligned with the experimental data.

The thermochemical (chemical potential/molar Gibbs energy) and electronic parameters (HOMO and LUMO energies) of **3**, **3'** and **Zn-3** were compared to analyze their

relative stabilities (Table 1). The chemical potential (μ) of *meso*-hydroxy dipyrromethane **3** was calculated to be 11.57 eV, higher than that of dipyrrin **3'** (10.90 eV). This indicated that dipyrrin **3'** was thermochemically more stable than **3**, making the conversion of **3'** to **3** thermochemically unfavorable. This stability explained the higher intensity of the dipyrrin signal observed in MALDI-TOF MS analysis.

In contrast, **Zn-3** exhibited a chemical potential (μ) of 10.74 eV, lower than that of **3**, suggesting that the complexation of 3 with zinc(II) was thermochemically favorable. However, **3** showed the highest HOMO-LUMO gap (4.36 eV) compared to those of **3'** (3.00 eV) and **Zn-3** (2.54 eV), explaining that it was the most electronically stable structure. This higher electronic stability may contribute to the slow kinetics observed in the complexation of **3** with zinc(II) despite its thermochemical favorability.

Table 1. Calculated chemical potential, HOMO, and LUMO energies of the species from DFT calculations

Species	μ (eV)	HOMO (eV)	LUMO (eV)	HOMO-LUMO Gap (eV)
3	11.57	-6.14	-1.78	4.36
3'	10.90	-5.94	-2.94	3.00
Zn-3	10.74	-8.67	-6.13	2.54
2	11.50	-6.03	-1.67	4.35
2'	11.30	-8.66	-6.55	2.11
3-H$^+$	12.03	-8.44	-4.73	3.71
DDQ	0.61	-8.47	-5.19	3.28
DDQ-H	0.93	-1.93	1.30	3.23
DDQ-H$_2$	1.28	-7.15	-2.93	4.22
H$_2$O	0.08	-8.51	0.45	8.96
H$_3$O$^+$	0.41	-20.19	-7.53	12.66
4	7.98	-8.94	-6.28	2.66
5	4.30	-10.27	-7.18	3.09
6	5.33	-10.05	-6.77	3.28
7	10.27	-8.85	-6.87	1.98

To further study the formation of compound **3**, we examined the proposed mechanism for the oxidation of dipyrromethane and its side reactions, as shown in Fig. 9, following a pathway similar to that of a previously reported [14]. The first step involved a hydride transfer from dipyrromethane **2** to **DDQ**, producing the cationic intermediate dipyrromethane **2'** and **DDQ-H**. This intermediate was subsequently deprotonated by **DDQ-H**, leading to the formation of dipyrrin **3'** and reduced **DDQ** (**DDQ-H$_2$**). Additionally, the C-*meso* of intermediate **2'** was susceptible to nucleophilic attack, such as by water, which resulted in the formation of the side product *meso*-hydroxy dipyrromethane **3** after the deprotonation of the hydroxonium group.

The first step in the oxidation of dipyrromethane involved hydride transfer from dipyrromethane to the oxygen of **DDQ**, driven by a small chemical potential difference of 0.12 eV (Fig. 10). The second step showed that the main reaction involving deprotonation had a lower chemical potential difference (0.04 eV) than the side reaction (0.66 eV). Thus, side reaction produced thermochemically less stable products.

The reactivity of these pathways can be explained by the interaction between filled and empty molecular orbitals. In the main reaction, the deprotonation of the N-H group in the cationic dipyrromethane intermediate (**2'**) by **DDQ-H** involves an orbital interaction between the non-bonding orbital of oxygen in **DDQ-H** (HOMO-1) and the anti-bonding σ orbital of H-N in **2'** (LUMO+10) with an energy difference of 1.24 eV (Fig. 11). In contrast, the side reaction involves a nucleophilic attack by water. This occurs through the interaction between the non-bonding orbital of oxygen in H_2O (HOMO) and the empty *p* orbital of **2'** (LUMO) with a much larger energy difference of 1.96 eV. Although the main reaction is more favorable, the relatively low energy barrier for the side reaction suggests its significance, particularly in the presence of water.

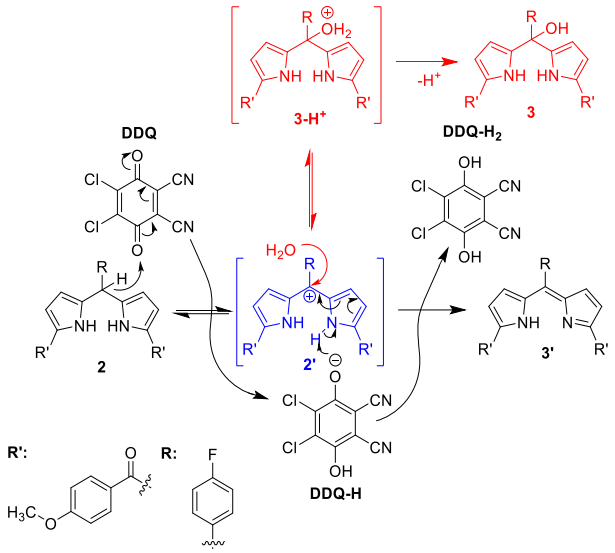

Fig. 9. Proposed mechanism of dipyrromethane **2** oxidation

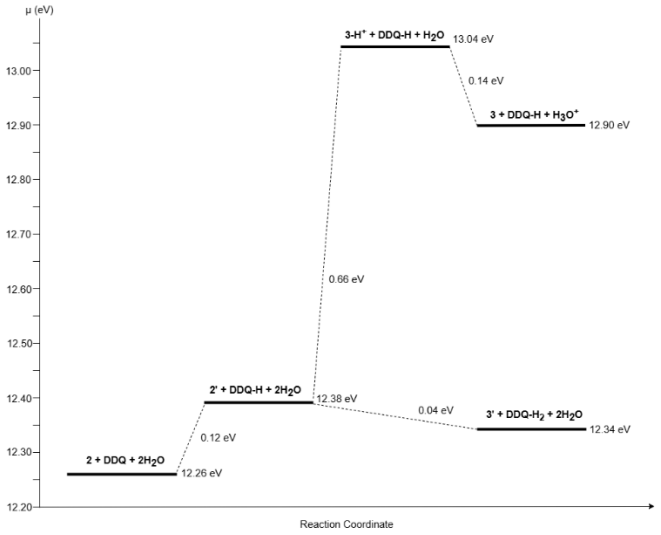

Fig. 10. Energy diagram of DPM oxidation

To determine the role of *p*-fluorophenyl and diacyl substituents in the competitiveness of the main (N-H deprotonation) and side (H_2O attack) reaction pathways, we performed similar computational calculations with *meso*-substituted dipyrromethane derivatives as previously reported [12,26]. Across the series of these *meso*-substituted dipyrromethane cations (compounds **2'**, **4-7**; see Fig. 12 for structures), the calculated energy gaps (Table 2) indicated that N-H deprotonation overall became the more favorable pathway since the N-H deprotonation gaps (E_2) consistently were lower than the corresponding water attack gaps (E_1). The DPM cation bearing a *meso*-pentafluorophenyl (C_6F_5) substituent (compound **5**) exhibited lower E_2 (0.72 eV) than the electron-rich **4** (1.22 eV) and *p*-fluorophenyl substituent (compound **6**,

0.9 eV), resulting in more dominant N-H deprotonation. However, dipyrrin of compound **4** can also be obtained experimentally, rationalized by significantly higher E_1 = 2.23 eV compared to E_2 = 1.22 eV, resulting in higher ΔE = 1.01 eV, diminishing the competitiveness of water attack. *p*-Fluorophenyl (*p*-F) substituent uniquely exhibited dual electronic influence, inductively withdrawing-electron and mesomerically electron-donating effect, leading to intermediate energy gaps (E_1 = 1.74 eV and E_2 = 0.90 eV, ΔE = 0.84 eV). On the other hand, the addition of diacyl groups (**2'** vs. **6** and **7** vs. **5**) increased E_2 and decreased ΔE, resulting in a higher possibility of water attack. These trends suggest that the electronic properties and diacyl groups play an essential role in *meso*-hydroxy DPM formation.

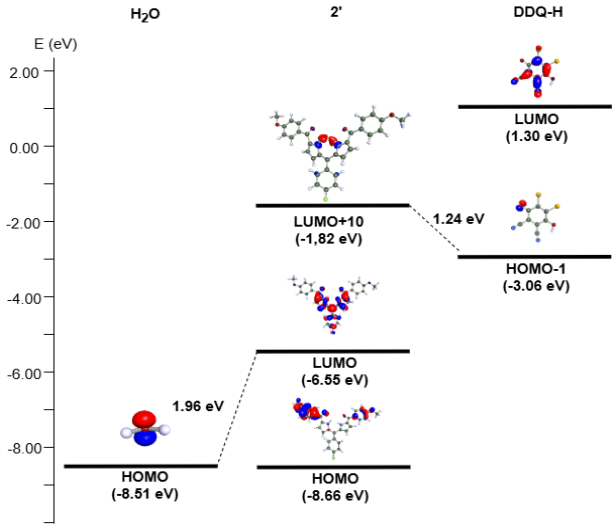

Fig. 11. Energy diagram of molecular orbital in the oxidation reaction of dipyrromethane **2**

Table 2. Electronic energy gap analysis of cationic dipyrromethane species and their interactions with H_2O and DDQ-H

cations	E_{LUMO} (eV)	$E_{\sigma^* N\text{-}H}$ (eV)	E_1 (eV)	E_2 (eV)	$\Delta E = E_1 - E_2$ (eV)
2'	−6.55	−1.82 (LUMO+10)	1.96	1.24	+0.72
4	−6.28	−1.84 (LUMO+8)	2.23	1.22	+1.01
5	−7.18	−2.34 (LUMO+8)	1.33	0.72	+0.61
6	−6.77	−2.16 (LUMO+7)	1.74	0.9	+0.84
7	−6.87	−1.9 (LUMO+11)	1.64	1.16	+0.48

E_1: gap energy between unoccupied *p* orbital (LUMO) of C-*meso* of cationic dipyrromethane species with HOMO of H_2O.

E_2: gap energy between σ* N-H orbital of C-*meso* of cationic dipyrromethane species with *n* O orbital (HOMO-1) of DDQ-H (-3.06 eV).

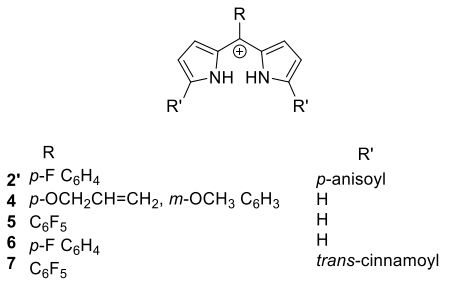

	R	R'
2'	*p*-F C_6H_4	*p*-anisoyl
4	*p*-$OCH_2CH{=}CH_2$, *m*-OCH_3 C_6H_3	H
5	C_6F_5	H
6	*p*-F C_6H_4	H
7	C_6F_5	*trans*-cinnamoyl

Fig. 12. Structure of *meso*-substituted dipyrromethane cation derivatives

4. Conclusion

Meso-hydroxy acyl dipyrromethane **3** was synthesized and characterized to investigate its stability and formation mechanism. The compound was obtained in the yield of 21% and fully identified by NMR and HRMS analyses. UV-vis absorption studies demonstrated that the *meso*-hydroxy group in **3** disrupted the conjugated system, resulting in a λ_{max} of 325 nm. Upon the addition of zinc(II) ions, a typical zinc(II)-dipyrrin complex was formed, exhibiting a bathochromic shift to 567 nm and an emission peak at 606 nm. Thermochemical stability analyses revealed that dipyrrin **3'** was more stable than *meso*-hydroxy dipyrromethane **3**. Although the complexation of **3** with zinc(II) was thermochemically favorable, it occurred more slowly than the complexation of dipyrrin. Mechanistic studies showed that the main oxidation pathway yielded dipyrrin **3'**, whereas a concurrent side reaction with water formed *meso*-hydroxy dipyrromethane **3**. Computational studies revealed that the competitiveness of these reaction pathways was modulated by substituent effects. The electron rich meso-substituent increased the energy for N-H deprotonation, whereas the diacyl groups lowered the ΔE (E_1 – E_2) for water attack. This study highlights the potential of the *meso*-hydroxy DPM fluorescence ligand for zinc(II) ions and the strategy to obtain the desired oligopyrrole.

Acknowledgements

The experiments resulting in this report are supported by International Research ITB 2022 (grant no. 4949/IT1.B07.1/TA.00/2022) under LPPM ITB. The authors are also grateful to FMIPA, ITB, Central Laboratory for NMR data and Physical Chemistry Division for emission spectroscopy.

References

1. Y. Ding, Y. Tang, W. Zhu and Y. Xie, *Fluorescent and colorimetric ion probes based on conjugated oligopyrroles,* Chem. Soc. Rev. 44 (2015) 1101–1112
2. E. V. Antina, N. A. Bumagina, A. I. V'yugin and A. V. Solomonov, *Fluorescent indicators of metal ions based on dipyrromethene platform*, Dyes Pigm. 136 (2017) 368–381
3. N. Boens, B. Verbelen, M. J. Ortiz, L. Jiao and W. Dehaen, *Synthesis of BODIPY dyes through postfunctionalization of the boron dipyrromethene core*, Coord. Chem. Rev. 399 (2019) 213024
4. R. S. Singh, R. P. Paitandi, R. K. Gupta and D. S. Pandey, *Recent developments in metal dipyrrin complexes: Design, synthesis, and applications,* Coord. Chem. Rev. 414 (2020) 213269.
5. P. Kaur and K. Singh, *Recent advances in the application of BODIPY in bioimaging and chemosensing*, J. Mater. Chem. C 7 (2019) 12040-12047.
6. M. C. Malacarne, M. B. Gariboldi and E. Caruso, *BODIPYs in PDT: A Journey through the Most Interesting Molecules Produced in the Last 10 Years*, Int. J. Mol. Sci. 23 (2022) 10198.
7. G. Li, K. Hu, C. Yi, K. L. Knappenberger Jr., G. J. Meyer, S. I. Gorelsky and M. Shatruk, *Panchromatic light harvesting and hot electron injection by Ru(II) dipyrrinates on a TiO_2 surface*, J. Phys. Chem. C 117 (2013) 17399-17411.

8. G. Li, K. Hu, K. C. D. Robson, S. I. Gorelsky, G. J. Meyer, C. P. Berlinguette and M. Shatruk, *Tris-Heteroleptic Ruthenium–Dipyrrinate Chromophores in a Dye-Sensitized Solar Cell*, Chem. Eur. J. 21 (2015) 2173-2181.
9. T. E. Hewat, L. J. Yellowlees and N. Robertson, *Neutral copper(I) dipyrrin complexes and their use as sensitizers in dye-sensitized solar cells*, Dalton Trans. 43 (2014) 4127-4136.
10. M. Yadav, A. K. Singh, R. Pandey and D. S. Pandey, *Synthesis and characterization of complexes imparting N-pyridyl bonded meso-pyridyl substituted dipyrromethanes*, J. Organomet. Chem. 695 (2010), 841–849.
11. S. Majumder and A. L. Odom, *Group-4 dipyrrolylmethane complexes in intramolecular olefin hydroamination*, Organometallics 27 (2008) 1174–1177.
12. D. Firmansyah, D. S. Qolby, L. D. Juliawaty and B. Yuliarto, *Cinnamoyl Dipyrromethenes as Fluorescence Zinc(II) Ion Sensor,* Chem. Asian J. 18 (2023) e202300187.
13. Y. Ding, X. Li, T. Li, W. Zhu and Y. Xie, *α-Monoacylated and α,α'- and α,β'-Diacylated Dipyrrins as Highly Sensitive Fluorescence "Turn-on" Zn^{2+} Probes*, J. Org. Chem. 78 (2013) 5328–5338.
14. Y. Ding, T. Li, X. Li, W. Zhu and Y. Xie, *From nonconjugation to conjugation: novel meso-OH substituted dipyrromethanes as fluorescence turn-on Zn^{2+} probes*, Org. Biomol. Chem. 11 (2013) 2685-2692
15. Y. Tang, Y. Ding, X. Li, H. Ågren, T. Li, W. Zhang and Y. Xie, *Acylation of dipyrromethanes at the α and β positions and further development of fluorescent Zn^{2+} probes*, Sens. Actuators B Chem. 206 (2014) 291–302.
16. M. E. Khatib, A. V. Cheprakov, and S. A. Vinogradov, *Unusual reactivity and metal affinity of Water-Soluble dipyrrins*, Inorg. Chem. 61 (2022) 12746–12758.
17. B. J. Littler, M. A. Miller, C.-H. Hung, R. W. Wagner, D. F. O'Shea, P. D. Boyle and J. S. Lindsey, *Refined Synthesis of 5-Substituted Dipyrromethanes*, J. Org. Chem. 64 (1999) 1391-1396.
18. Q. Wang, Y. Xie, Y. Ding, X. Li, and W. Zhu, *Colorimetric fluoride sensors based on deprotonation of pyrrole–hemiquinone compounds*, Chem. Commun. 46 (2010) 3669–3671.
19. C. Steffen, K. Thomas, U. Huniar, A. Hellweg, O. Rubner, and A. Schroer, *TmoleX—A graphical user interface for TURBOMOLE*, J. Comput. Chem. 31 (2010) 2967–2970.
20. S. G. Balasubramani, et al., *TURBOMOLE: Modular program suite for ab initio quantum-chemical and condensed-matter simulations*, J. Chem. Phys. 152 (2020) 184107.
21. C. Bannwarth, S. Ehlert and S. Grimme, *GFN2-xTB—An Accurate and Broadly Parametrized Self-Consistent Tight-Binding Quantum Chemical Method with Multipole Electrostatics and Density-Dependent Dispersion Contributions*, J. Chem. Theory Comput. 15 (2019) 1652–1671.
22. A. D. Becke, *Density-functional thermochemistry. III. The role of exact exchange*, J. Chem. Phys. 98 (1993) 5648–5652.
23. P. J. Stephens, F. J. Devlin, C. F. Chabalowski and M. J. Frisch, *Ab Initio Calculation of Vibrational Absorption and Circular Dichroism Spectra Using Density Functional Force Fields*. J. Phys. Chem. 98 (1994) 11623–11627.
24. A. Schäfer, C. Huber and R. Ahlrichs, *Fully optimized contracted Gaussian basis sets of triple zeta valence quality for atoms Li to K,* J. Chem. Phys. 100 (1994) 5829–5835.
25. M. B. Huda, Nurlelasari, W. Safriansyah, M. Fajar, I. I. Widiyowati, U. Supratman, Y. Permana, and Y. P. Budiman, *One pot two-step borylation/fluorination reaction of dysobinin from Chisocheton macrophyllus and its cytotoxicity against cancer cell*, Commun. Sci. Technol. 9 (2024) 366–371.
26. D. Firmansyah, A. T. Khodizah, M. A. Ferryansyah, I. M. Divananda, L. D. Juliawaty, D. Mujahidin, B. Yuliarto, N. Ishikawa, and A. Santria, *Spectroscopic and computational study of vanillin-dipyrrin ligand that capable of colorimetric sensor for zinc and copper ions*, J. Mol. Struct. 1313 (2024) 138718.